Proc. Natl. Acad. Sci. USA
Vol. 96, pp. 10422–10427, August 1999
Neurobiology, Applied Physical Sciences

Tracking neuronal fiber pathways in the living human brain

THOMAS E. CONTURO*†¶, NICOLAS F. LORI*†, THOMAS S. CULL*, ERBIL AKBUDAK*, ABRAHAM Z. SNYDER*, JOSHUA S. SHIMONY*, ROBERT C. MCKINSTRY*, HAROLD BURTON*‡, AND MARCUS E. RAICHLE*§‡

*Department of Radiology and Neuroimaging Laboratory, Mallinckrodt Institute of Radiology and Departments of §Neurology and ‡Anatomy and Neurobiology, Washington University School of Medicine, 4525 Scott Avenue, St. Louis, MO 63110; and †Department of Physics, Washington University, One Brookings Drive, St. Louis, MO 63130

Contributed by Marcus E. Raichle, July 12, 1999

ABSTRACT **Functional imaging with positron emission tomography and functional MRI has revolutionized studies of the human brain. Understanding the organization of brain systems, especially those used for cognition, remains limited, however, because no methods currently exist for noninvasive tracking of neuronal connections between functional regions [Crick, F. & Jones, E. (1993) *Nature (London)* 361, 109–110]. Detailed connectivities have been studied in animals through invasive tracer techniques, but these invasive studies cannot be done in humans, and animal results cannot always be extrapolated to human systems. We have developed noninvasive neuronal fiber tracking for use in living humans, utilizing the unique ability of MRI to characterize water diffusion. We reconstructed fiber trajectories throughout the brain by tracking the direction of fastest diffusion (the fiber direction) from a grid of seed points, and then selected tracks that join anatomically or functionally (functional MRI) defined regions. We demonstrate diffusion tracking of fiber bundles in a variety of white matter classes with examples in the corpus callosum, geniculo-calcarine, and subcortical association pathways. Tracks covered long distances, navigated through divergences and tight curves, and manifested topological separations in the geniculo-calcarine tract consistent with tracer studies in animals and retinotopy studies in humans. Additionally, previously undescribed topologies were revealed in the other pathways. This approach enhances the power of modern imaging by enabling study of fiber connections among anatomically and functionally defined brain regions in individual human subjects.**

Knowledge of the link between functional brain regions and anatomical fiber connections is essential to an integrated understanding of the organization of the human nervous system. Optimally, both functional domains and their anatomical connections would be mapped in the same subject. The pathways involved in specific functions could thereby be inferred and hypotheses about brain networks formulated and tested. This combined approach has established the complex organization of the nonhuman primate visual system (1). In humans, positron emission tomography (2, 3) and functional MRI (fMRI) (4–6) have provided considerable insight into regional functional specialization, especially for cognitive tasks. However, an understanding of connections between activated regions in humans relies on older, and admittedly impoverished (7), descriptions of gross dissections (e.g., ref. 8) or clinical-pathological correlations (e.g., ref. 9), the latter often based on stained patterns of demyelination (10). Connectional studies in animals use a variety of invasive tracer injections (e.g., refs. 11, 12–18) that cannot be performed in humans. Animal studies also yield limited information regarding human cognitive functions such as language or pathological conditions such as psychiatric disorders. Passive diffusive tracer studies of the postmortem human brain [e.g., by using 1,1′-dioctadecyl-3,3,3′,3′-tetramethylindocarbocyanine (17)] require months to trace very short distances (≈mm) and are affected by crossfiber diffusion. Some information on human fiber trajectories can be obtained by imaging fiber degeneration (19) but only in pathologic cases and in selected fiber pathways. The ability to track white matter fibers noninvasively in humans would enable comparison of structural differences in brain organization between subjects in normal and abnormal states and enable study of potential fiber connections between functional brain regions.

By using the general principle that brain water preferentially diffuses in the direction of white matter fibers (20–22), we computationally traced neuronal fiber bundles in human subjects with optimized diffusion tensor-encoded MRI (DT-MRI) (23–25). This procedure monitors rapid microscopic ($\approx\mu$m) self-diffusive water movements rather than slow macroscopic (≈mm) tracer displacements. From $1.25 \times 1.25 \times 2.5$ mm image data acquired in a 2-hr session, we reconstructed diffusion tracks throughout the brain by repeatedly stepping along the direction of fastest diffusion, starting from a 1-mm grid of seed points covering the entire brain. We then identified subsets of tracks that linked regions initially selected on the basis of anatomical landmarks or fMRI activated foci. Results were obtained in commissural and projection systems where anisotropy is high (26) and fibers are highly parallel and in more complex association fiber systems having relatively low anisotropy (26). Prior studies that used diffusion imaging evaluated trajectory data only in limited regions acquired from excised fixed rat brain with long scan times (27).

METHODS

Diffusion Tensor Analysis. In DT-MRI a set of water self-diffusion coefficients (D) are measured by sensitizing the magnetic resonance (MR) signal to random motions by using strong magnetic field gradients. Determining D from the sensitized MR signal equates to measuring the root-mean-square displacement of diffusing water. Diffusion is anisotropic in white matter fiber bundles, being faster along the fiber direction (20, 21). For MR fiber tracking, anisotropic diffusion is characterized to determine the preferred diffusion direction. In anisotropic media, the displacement "front" of a diffusing substance has an ellipsoid shape (23, 25, 28). Each D measurement defines a displacement to a point on the ellipsoid surface along the direction of the sensitizing gradient. Acquiring MR data by using different gradient orientations allows sampling of enough points on the ellipsoid surface to define the ellipsoid uniquely (i.e., only one ellipsoid would fit all

The publication costs of this article were defrayed in part by page charge payment. This article must therefore be hereby marked "*advertisement*" in accordance with 18 U.S.C. §1734 solely to indicate this fact.

PNAS is available online at www.pnas.org.

Abbreviations: MR, magnetic resonance; DT-MRI, diffusion tensor-encoded MRI; fMRI, functional MRI; 3D, three-dimensional; 2D, two-dimensional; LGN, lateral geniculate nucleus.

¶To whom reprint requests should be addressed. E-mail: tconturo@npg.wustl.edu.

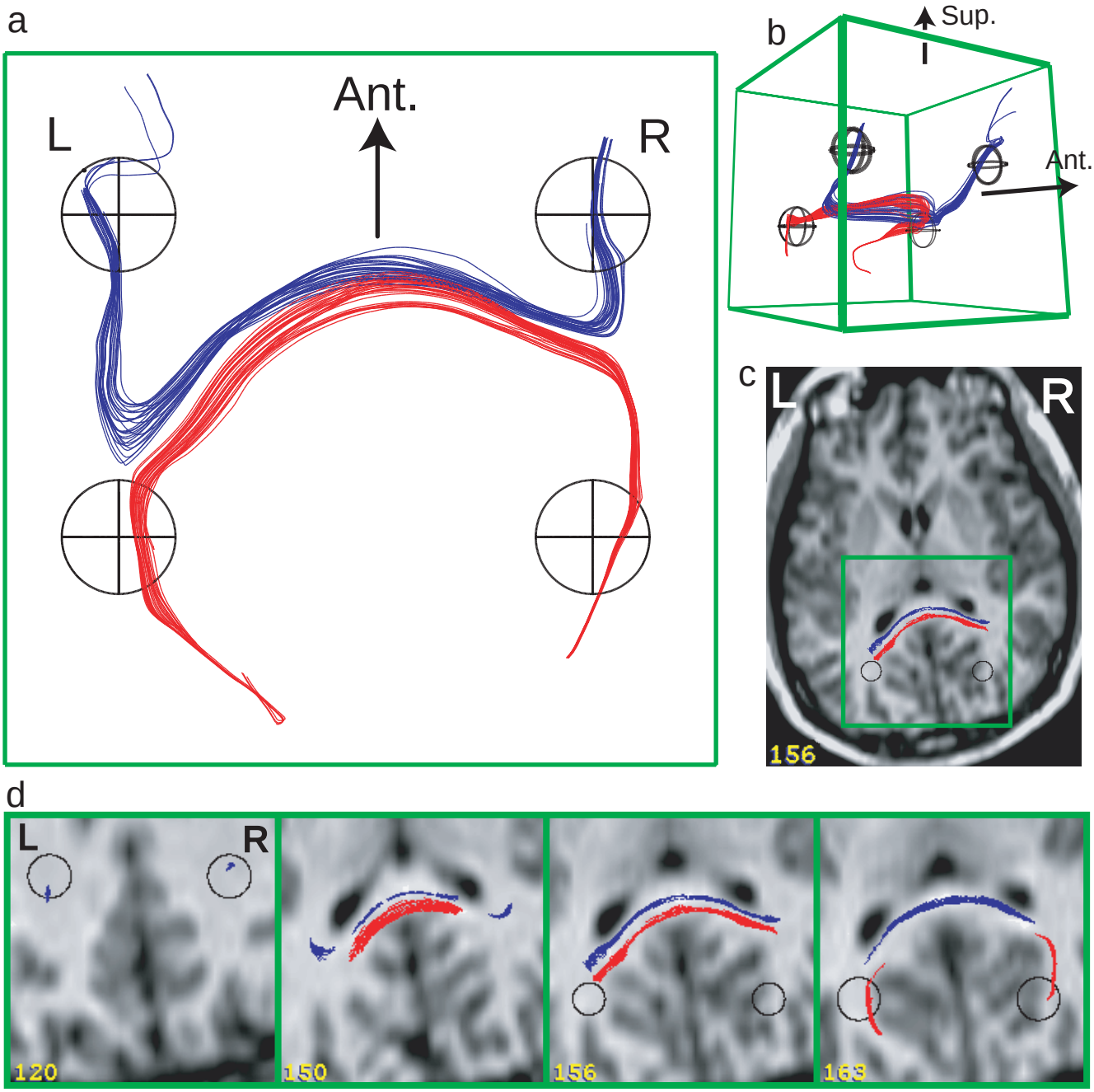

FIG. 1. Diffusion tracking of commissural fibers. 3D projection views (*a* and *b*) of diffusion tracks (red and blue) in the splenium of the corpus callosum selected with ellipsoid filtering volumes (black). Tracks are viewed from above (*a*) and from the anterior-right direction (*b*). In *c*, the general anatomical location of tracks and ellipsoids is shown in 2D overlay (see *Methods*) on a brain slice that cuts through the splenium (T1-weighted slice 156). Magnified 2D overlays (*d*) of tracks and ellipsoids onto selected slices (interpolated slices numbered superior-to-inferior with 24 slices/cm). The green boxed region surrounding the 3D projections (*a* and *b*) corresponds to the green squared regions on 2D anatomical overlays (*c* and *d*). Tracks were selected by ellipsoid filtration of whole-brain diffusion data (computed at an anisotropy threshold of $A_\sigma \geq 0.19$). Tracks that passed through the splenium were observed to divide into two groups laterally and were color coded based on passage into lateral ellipsoids (black circles on all images). Tracks projected to the occipital lobes (red tracks) and parietal lobes (blue tracks), and had a topological relation within the splenium best seen in *a* and slice 156 in *d*. The oblique 3D view (*b*) shows the more superior projection of the parietal tracks (blue). Tracks were thinned by a factor of 8 for 3D display.

points in the absence of noise) (23–25, 29). Associated with a given ellipsoid is a symmetric 3×3 diffusion tensor (**D**) having three eigenvectors (the ellipsoid axes) and three eigenvalues (D along these axes). The eigenvector corresponding to the largest eigenvalue is the direction of fastest diffusion and indicates fiber direction.

DT-MRI and Anatomical MRI. Single-shot echo-planar (30) imaging pulse sequences with diffusion tensor encoding were implemented on a Siemens Vision 1.5 Tesla MR system (Erlangen, Germany). We applied Stejskal–Tanner diffusion-sensitizing gradients (31) along four tetrahedral and three orthogonal directions (25, 26) and acquired contiguous multislice images (45–51 slices, 2.5-mm isotropic voxels reconstructed to $1.25 \times 1.25 \times 2.5$-mm pixels) in four normal male human subjects (24–49 yr). Image acquisition was repeated up to 10 times in each subject for averaging (29-min total scan time). Anatomical images weighted by the longitudinal relaxation time (T1) were also acquired (2-hr total session, includ-

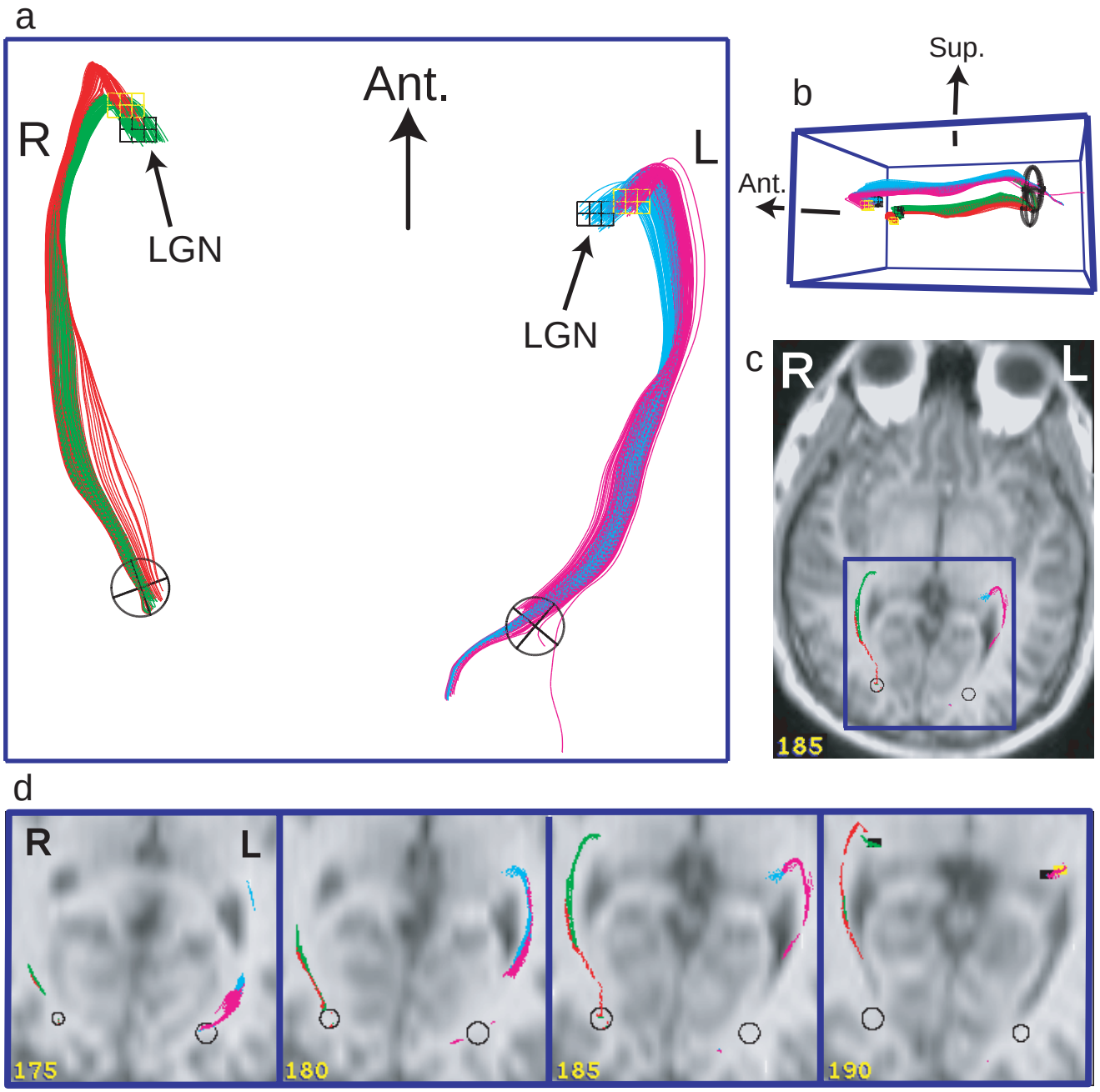

FIG. 2. Diffusion tracking of the geniculo-calcarine tracts. 3D projections (*a* and *b*) of tracks and filtering volumes (ellipsoids and small cubes) are viewed directly from below (*a*) and obliquely from the left (*b*). In *c*, the general anatomical location is shown in 2D overlay on one brain slice (slice 185) that was located near the midportion of the splenium. The detailed anatomical location is shown in magnified 2D overlay in *d*. The dark blue boxed regions correspond on all images. Tracks were anatomically selected from whole-brain track data ($A_\sigma \geq 0.14$ threshold, same subject as Fig. 1). Tracks were retained that entered the ellipsoidal volumes located adjacent to visual cortex (lateral to the calcarine fissure) and the ipsilateral LGN volumes (cubes) manually drawn based on thalamic contours. LGN volumes were separated into medial (black cubes) and lateral (yellow cubes) parts for analysis of topology. A medial-lateral topology is demonstrated from the LGN to the optic radiations (best seen in *a*), and a superior-inferior topology is revealed along the length of the geniculo-calcarine tract (best seen in *b*).

ing DT-MRI image reconstruction and anatomical MRI). We realigned DT-MRI images, computed absolute total diffusion anisotropy (A_σ) (25) to assess the directional strength of diffusion, and registered anatomical and fMRI images to DT-MRI data (32, 33). Anatomical data were resampled to isotropic 1.25-mm voxels to define filtering regions and to 0.42-mm voxels for anatomical overlays (see below).

Diffusion Track Reconstruction and Display. *Single diffusion tracks* were reconstructed by bidirectionally following the direction of fastest diffusion, in 0.5-mm steps, starting from an initial location (seed point) to a termination point. Tracks were terminated where A_σ fell below an assigned threshold (the trackability threshold), typically in gray matter. The tensor **D** and its eigenvector corresponding to the largest eigenvalue were calculated (26) at each step, from interpolated DT-MRI data, to define the direction of the next step. A *whole-brain track data set* was produced by repeating this procedure for every seed point above the trackability threshold in a 1.0-mm cubic grid of seed points. *Groups of diffusion tracks* were selected by extracting from the whole-brain track data only those tracks that entered given volumes of interest. This "filtering" procedure used either anatomical regions (ellipsoidal or manually traced) or thresholded fMRI activations. Tracks were displayed in three-dimensional (3D) projections

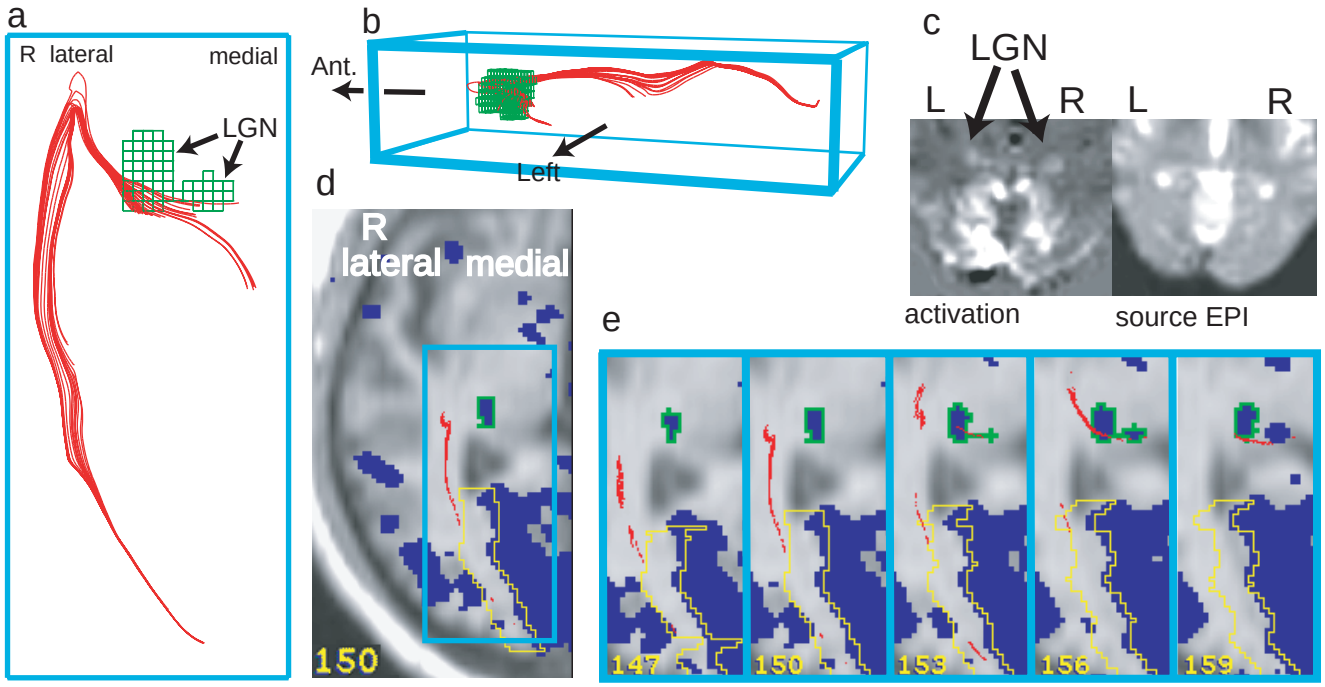

FIG. 3. Functional selection of geniculo-calcarine diffusion tracks by using fMRI activations (different subject from Fig. 1; $A_\sigma \geq 0.11$). 3D projection views (*a* and *b*) of tracks (red) and fMRI-defined LGN filtering volumes (green) viewed directly from below (*a*) and from the left (*b*). In *c*, the visual cortex and LGN were activated by visual stimulation (unthresholded fMRI subtraction image is displayed above the corresponding source echo-planar image). Functional selection of tracks (*d* and *e*) used activated LGN and visual cortex regions. Tracks were selected anteriorly based on passage into the LGN volume (green outline), which was traced from the total activation thresholded at ≥0.22% signal change (blue region). Tracks were selected posteriorly in the occipital lobe based on passage into a border region (yellow), which was constructed as a 1-cm band lateral to the activation in medial occipital cortex (thresholded at ≥0.41%). Border filtration was implemented because of the absence of spatial overlap between tracks and visual cortex activation (where tracks terminated at white matter borders and activations were confined to gray matter).

viewed from two different directions. In cases of overlap, background tracks were hidden by foreground tracks. In some 3D projections, tracks were randomly removed by a designated thinning factor to better display dense track structure. Precise anatomical track location was evaluated by two-dimensional (2D) overlay of tracks and filtering volumes onto T1-weighted anatomical slices, displaying only track segments that were within the slices. 3D projections were viewed in MATLAB (Mathworks, Natick, MA), and 2D overlays were viewed in ANALYZE (Mayo Foundation, Rochester, MI).

fMRI. fMRI was performed in a different imaging session by using contiguous multislice single-shot asymmetric spin-echo echo-planar imaging as described (33). Four runs of 128-frame fMRI data (2.36 s per frame) were collected during photic stimulation (Grass Instruments, Quincy, MA). Stimuli were presented in 21.2-s blocks alternating with 21.2-s control periods. Images were realigned within and across runs, control images were subtracted from task images, and fMRI data were coregistered to DT-MRI data in the same subject.

RESULTS AND DISCUSSION

Diffusion tracks were traced along the highly ordered commissural fiber bundles of the splenium of corpus callosum (Fig. 1) that connect posterior aspects of the two cerebral hemispheres. Consistent with known anatomy (e.g., Fig. 214 in ref. 34), tracks paralleled the curvature of the splenium and divided laterally to course across several slices into the occipital lobe (forceps major, red tracks) and parietal lobe (blue tracks). These results also suggest a previously undescribed radial topology wherein the projections headed for occipital cortex segregate into the outer portion of the splenium (best seen in slice 156 in Fig. 1, which is a cross-sectional slice through the midportion of the splenium).

Diffusion tracks were followed over longer distances in the highly anisotropic geniculo-calcarine visual pathways that relay visual information from the thalamus to the visual cortex. Diffusion tracks were selected by placing filtering regions in the lateral geniculate nucleus (LGN) of the thalamus and adjacent to visual cortex by using anatomical landmarks (Fig. 2). The resulting tracks were consistent with anatomical descriptions of the geniculo-calcarine tract based on gross dissections, clinical-pathologic correlations, and animal tracer studies (for review, see pp. 181 and 244 in ref. 34 and pp. 585–588 in ref. 35). Tracks exited from the LGN in an anterior-superior direction and passed immediately lateral to the occipital horns of the lateral ventricles (see 2D overlays). As shown by color coding, trajectories from different portions of the LGN were separated along their course to the visual cortex and had a characteristic topology. Tracks from the lateral-inferior part of the LGN (magenta and red groups in Fig. 2) passed anteriorly into the temporal lobe, around the loop of Meyer, and into the optic radiations. Tracks from the medial-superior part of the LGN more directly entered the optic radiations, passing posterior and superior to the loop of Meyer (green and cyan groups). The two trajectories maintained a superior-inferior relation along the entire length of the geniculo-calcarine tract (best seen in Fig. 2*b*) in agreement with invasive studies in animals (see p. 588 of ref. 35 for review). The two trajectories also had a medial-lateral relation along the anterior half of the geniculo-calcarine tract, from the LGN to the optic radiations immediately lateral to the lateral ventricles (best seen in Fig 2*a*). The lateral part of the LGN projected to the inferior part of the visual cortex in agreement with the known retinotopy of the upper visual field in humans (36, 37). Comparable results were obtained by defining filtering regions based on fMRI activation foci (Fig. 3), where the tracks have a precise projection to the center of the activation

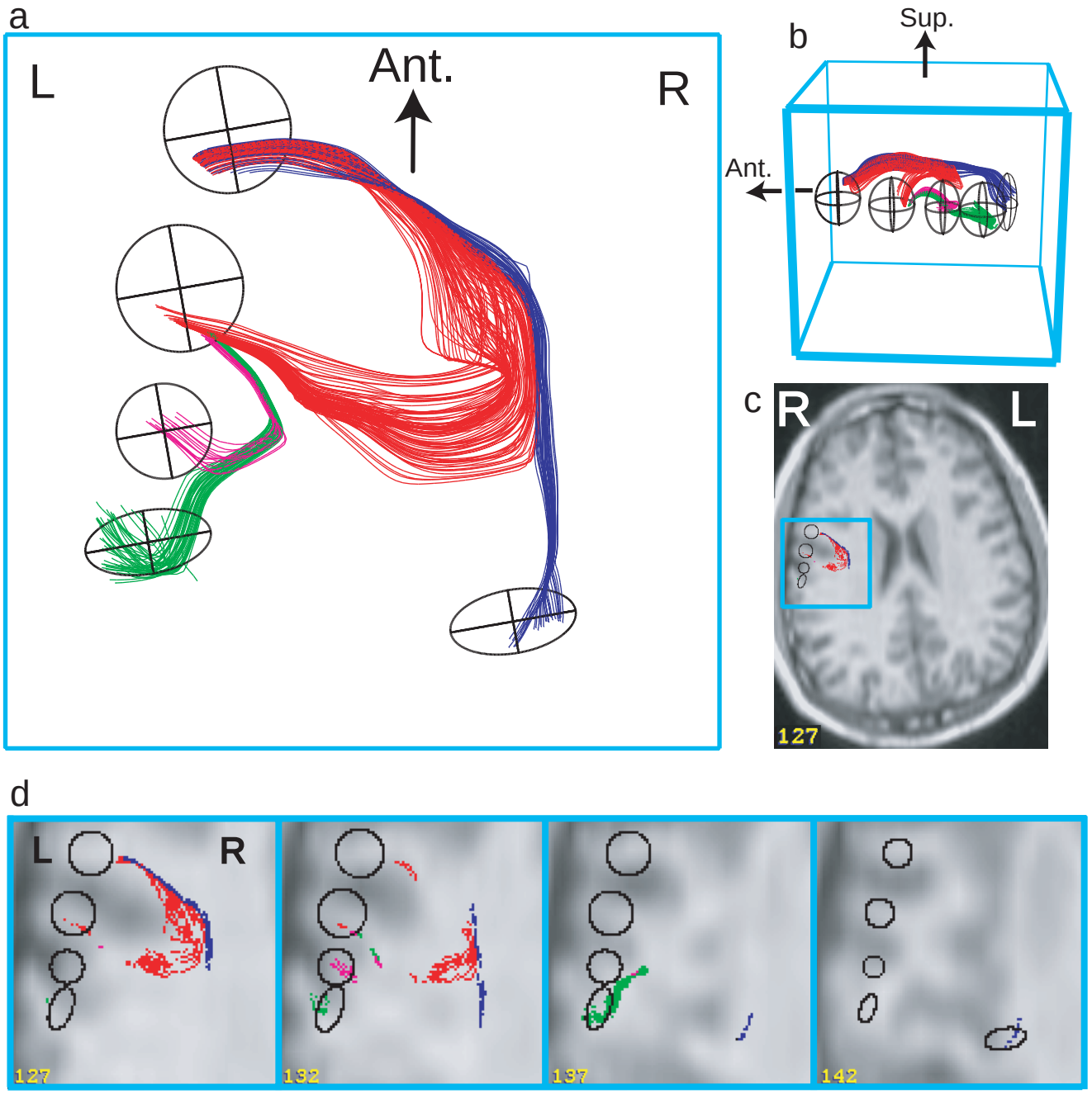

FIG. 4. Diffusion tracking of parietal association fibers (same subject as Fig. 1; $A_\sigma \geq 0.11$). 3D projections (*a* and *b*) are viewed directly from above (*a*) and from the left-superior direction (*b*). In *c*, a 2D anatomical overlay onto one whole brain slice (#127) demonstrates general anatomical location. Magnified 2D overlays (*d*) demonstrate the fine anatomical location of tracks and filtering ellipsoids. Tracts were anatomically selected as those that entered paired combinations of five ellipsoids (black), four located in subcortical white matter, and one positioned in deep white matter. Of the 10 possible paired filtering combinations, the top four combinations (displayed) yielded 93% of the tracks (107 red, 44 green, 31 blue, and 15 magenta tracks). Three of the combinations yielded zero tracks. The blue tracks end in a region of below-threshold anisotropy in deep white matter.

in primary visual cortex where visual information is directly received.

Lastly, we tracked association fiber bundles connecting nearby cortical regions. Results in the parietal lobe (Fig. 4) show the feasibility of diffusion tracking in the more complexly connected association systems having relatively low anisotropy (26). Tracks that connected adjacent gyri had tightly curved trajectories consistent with U-fibers (red and magenta tracks in Fig. 4), whereas tracks that traversed more distant gyri had a more complex trajectory (green tracks). Tracks also entered deep cortical white matter (blue tracks), immediately lateral to the corona radiata, compatible with long association tracks described in gross dissections and animal tracer studies (for review, see p. 800 in ref. 35 and p. 365 in ref. 34). A previously undescribed topology was exhibited whereby tracks connecting distant gyri layered medially as they converged along tracks connecting adjacent gyri (e.g., note green-magenta and blue-red layerings).

There are two main limitations to the current fiber tracking methods. First, tracking into cortical gray matter is compromised by the low anisotropy in gray matter. Gray matter anisotropy was not statistically above background noise for an average of two DT-MRI acquisitions (26). In the future, however, more extensive signal averaging might reveal detect-

able anisotropy in gray matter. We presently overcame this limitation by selecting tracks that approached within a distance of activated cortex (Fig. 3), but such a procedure may reduce selectivity. A second limitation is that the spatial resolution of DT-MRI data will likely affect the ability to track small and complexly arranged fiber bundles. In MRI, spatial resolution depends on signal-to-noise ratio (SNR) and acquisition time. By defining the limits in fiber bundle size and configuration trackable at specific SNR levels and spatial resolutions, the DT-MRI data collection could be adjusted to the desired degree of detail.

CONCLUSION

In summary, by using diffusion tensor imaging in living human subjects, we reconstructed representations of fiber trajectories of varied complexity and with differing levels of anisotropy. Tracks obtained in the commissural and thalamo-cortical projection systems had an overall shape consistent with classical anatomical descriptions. These tracks showed highly parallel and ordered arrays that revealed topologies compatible with animal tracer studies, as well as topologies not previously described. The patterning seen in tracking of local cortical association connections showed the potential for following greater complexities even where anisotropy is lower. In addition, we determined that diffusion tracking can be used to analyze the potential anatomical connections between functional domains. The approach presented herein combines functional and connectional assessment in individual subjects and should enable detailed study of the organization of brain systems in normal and abnormal living humans.

This work was supported in part by the Major Grants Program of the McDonnell Center for Higher Brain Function, the Charles A. Dana Foundation Consortium on Neuroimaging Leadership Training, and National Institutes of Health Grant P01 NS06833. We thank Thomas A. Woolsey and Joseph L. Price for review of the manuscript before submission and Robin K. Guillory for assistance with figures.

1. Felleman, D. J. & Van Essen, D. C. (1991) *Cereb. Cortex* **1,** 1–47.
2. Fox, P. T. & Raichle, M. E. (1986) *Proc. Natl. Acad. Sci. USA* **83,** 1140–1144.
3. Raichle, M. E. (1994) *Annu. Rev. Psychol.* **45,** 333–356.
4. Ogawa, S., Tank, D. W., Menon, R., Ellerman, J. M., Kim, S. G., Merkle, H. H. & Ugurbil, K. (1992) *Proc. Natl. Acad. Sci. USA* **89,** 5951–5955.
5. Kwong, K. K., Belliveau, J. W., Chesler, D. A., Goldberg, I. E., Weisskoff, R. M., Poncelet, B. P., Kennedy, D. N., Hoppel, B. E., Cohen, M. S., Turner, R., *et al*. (1992) *Proc. Natl. Acad. Sci. USA* **89,** 5675–5679.
6. Bandettini, P. A., Wong, E. C., Hinks, R. S., Tikofsky, R. S. & Hyde, J. S. (1992) *Magn. Reson. Med.* **25,** 390–397.
7. Crick, F. & Jones, E. (1993) *Nature (London)* **361,** 109–110.
8. Dejerine, J. (1895) *Anatomie des centres nerveux* (Rueff, Paris).
9. Critchley, M. (1966) *The Parietal Lobe* (Hafner, New York).
10. Ranson, S. (1943) *The Anatomy of the Nervous System* (Saunders, Philadelphia).
11. LaVail, J. H. (1975) *Fed. Proc.* **34,** 1618–1624.
12. Holstege, J. C. & Vrensen, G. F. (1988) *J. Microsc. (Oxford)* **150,** 233–243.
13. Steinbusch, H. W., Wouterlood, F. G., de Vente, J., Bol, J. G. & Berkenbosch, F. (1988) *Acta Histochem. Suppl.* **35,** 86–106.
14. Honig, M. G. & Hume, R. I. (1989) *Trends Neurosci.* **12,** 333–335, 340–341.
15. Veenman, C. L., Reiner, A. & Honig, M. G. (1992) *J. Neurosci. Methods* **41,** 239–254.
16. Ding, S. L. & Elberger, A. J. (1995) *J. Neurosci. Methods* **57,** 67–75.
17. Godement, P., Vanselow, J., Thanos, S. & Bonhoeffer, F. (1987) *Development (Cambridge, U.K.)* **101,** 697–713.
18. Burton, H. & Fabri, M. (1995) *J. Comp. Neurol.* **355,** 508–538.
19. Yagishita, A., Nakano, I., Oda, M. & Hirano, A. (1994) *Radiology (Easton, PA)* **191,** 455–460.
20. Moseley, M. E., Cohen, Y., Kucharczyk, J., Mintorovitch, J., Asgari, H. S., Wendland, M. F., Tsuruda, J. & Norman, D. (1990) *Radiology (Easton, PA)* **176,** 439–445.
21. Doran, M., Hajnal, J. V., Van Bruggen, N., King, M. D., Young, I. R. & Bydder, G. M. (1990) *J. Comput. Assist. Tomogr.* **14,** 865–873.
22. Makris, N., Worth, A. J., Sorensen, A. G., Papadimitriou, G. M., Wu, O., Reese, T. G., Wedeen, V. J., Davis, T. L., Stakes, J. W., Caviness, V. S., *et al*. (1997) *Ann. Neurol.* **42,** 951–962.
23. Basser, P. J., Mattiello, J. & Le Bihan, D. (1994) *J. Magn. Reson. B* **103,** 247–254.
24. Conturo, T. E., McKinstry, R. C., Aronovitz, J. A. & Neil, J. J. (1995) *NMR Biomed.* **8,** 307–332.
25. Conturo, T. E., McKinstry, R. C., Akbudak, E. & Robinson, B. H. (1996) *Magn. Reson. Med.* **35,** 399–412.
26. Shimony, J. S., McKinstry, R. C., Akbudak, E., Aronovitz, J. A., Snyder, A. Z., Lori, N. F., Cull, T. S. & Conturo, T. E. (1999) *Radiology (Easton, PA)* **212,** 770–784.
27. Mori, S., Crain, B. J., Chacko, V. P. & van Zijl, P. C. (1999) *Ann. Neurol.* **45,** 265–269.
28. Crank, J. (1975) *The Mathematics of Diffusion* (Clarendon, Oxford).
29. Basser, P. J. (1995) *NMR Biomed.* **8,** 333–344.
30. Mansfield, P. (1977) *J. Phys. C Solid State Phys*. **10,** L55–L58.
31. Stejskal, E. O. & Tanner, J. E. (1965) *J. Chem. Phys.* **42,** 288–292.
32. Ojemann, J. G., Buckner, R. L., Akbudak, E., Snyder, A. Z., Ollinger, J. M., McKinstry, R. C., Rosen, B. R., Petersen, S. E., Raichle, M. E. & Conturo, T. E. (1998) *Hum. Brain Mapp.* **6,** 203–215.
33. Corbetta, M., Akbudak, E., Conturo, T. E., Snyder, A. Z., Ollinger, J. M., Drury, H. A., Linenweber, M. R., Petersen, S. E., Raichle, M. E., Van Essen, D. C., *et al.* (1998) *Neuron* **21,** 761–773.
34. Nieuwenhuys, A., Voogd, J. & van Huijzen, C. (1988) *The Human Central Nervous System: A Synopsis and Atlas* (Springer, Berlin).
35. Brodal, A. (1981) *Neurological Anatomy* (Oxford Univ. Press, New York).
36. Jones, E. G. (1985) *The Thalamus* (Plenum, New York).
37. Walls, G. L. (1953) *Univ. Calif. Berkeley Publ. Physiol.* **9,** 1–100.